ORIGINAL RESEARCH ARTICLE

Local Composition Migration Induced Microstructural Evolution and Mechanical Properties of Non-equiatomic $Fe_{40}Cr_{25}Ni_{15}$ $Al_{15}Co_5$ Medium-Entropy Alloy

VIKAS SHIVAM, JOYSURYA BASU, R. MANNA, and N.K. MUKHOPADHYAY

A newly designed composition of non-equiatomic $Fe_{40}Cr_{25}Ni_{15}Al_{15}Co_5$ medium-entropy alloy (MEA) was produced by induction melting (IM). The as-cast alloy was found to consist of a two-phase microstructure of BCC (2.87 ± 0.01 Å) and ordered B2 (2.88 ± 0.02 Å) type phases. The structures of these phases were confirmed through X-ray diffraction (XRD) and transmission electron microscopy (TEM) techniques. It was observed that the Ni-Al-enriched ordered B2 phase of cuboidal shapes (~ 100 to 200 nm) is homogeneously distributed in Fe-Cr-rich BCC matrix with a cube-on-cube orientation relationship. The formation of the columnar dendrites (width 50 to 100 μm) was identified through optical microscopy (OM). The structural and microstructural stability of the alloy was investigated by heat-treating the alloy through different schedules. Heat-treated samples at different temperatures (< 1273 K) exhibit a similar type of two-phase microstructure with columnar dendrites. However, compositional rearrangement takes place during long time exposure to develop polymorphically related phases. The alloy was observed to possess a high compressive yield strength and hardness, *i.e.*, ~ 1047 MPa and 391 ± 9 HV, respectively, at room temperature. Heat-treated samples at 600 °C and 900 °C (873 K and 1173 K) showed an increase in yield strength and ultimate strength with a significant increase in plasticity due to the increase in volume fraction of B2 phase and softening of the BCC matrix phase. The thermal stability and high strength of this alloy may open new avenues for high-temperature applications.

https://doi.org/10.1007/s11661-021-06188-7

I. INTRODUCTION

THE last decade has witnessed a considerable resurgence in the development of the structure-property correlation of high-entropy alloys (HEAs).[1–4] Conventional alloys are based on one or two primary elements selected on the basis of the specific property requirements, and the other elements are added in minor proportions to augment the desired properties.[5] However, HEAs are designed to have five or more principal elements in equiatomic or near equiatomic concentration, varying in the range of 5 to 35 at. pct in order to have high configurational entropy in the range of 1.5R to 1.6R, where R is a universal constant.[6] HEAs have been processed through various processing routes, *e.g.*, melting/casting, solid state processing (*e.g.*, mechanical alloying), deposition techniques, and so on.[7–10] Melting/casting is the widely accepted route to produce bulk quantity of HEAs. The formation of various phases in HEAs depends on the alloy composition, processing methods and post-heat treatments. The phase transformation depends on the competition between the entropy and enthalpy to minimize the Gibbs free energy of an alloy[11–13] along with the kinetics of phase formation. Initial studies on HEAs relied on the effect of entropy leading to the formation of solid solution phases with relatively simpler crystal structures, *i.e.*, body-centered cubic (BCC), face-centered cubic (FCC) and hexagonal close-packed (HCP). However, it is interesting to point out that a small fraction of alloys only fulfill the composition requirement for a simple solid solution formation; thus, many HEAs have been reported to contain multiple phases and complex microstructures.[14] Consequently, many HEAs have been reported to have superior properties, *i.e.*, high strength, high hardness, good oxidation, corrosion and wear resistance, and high thermal stability, which qualify them as suitable materials for high-temperature applications.[12,15–19] It has

VIKAS SHIVAM, JOYSURYA BASU, R. MANNA, and N.K. MUKHOPADHYAY are with the Department of Metallurgical Engineering, Indian Institute of Technology (BHU), Varanasi, 221005, India. Contact e-mail: vikas.rs.met13@itbhu.ac.in
Manuscript submitted April 29, 2020; accepted February 7, 2021.
Article published online March 10, 2021

been observed that the formation of intermetallic phases often competes with the simple solid solution phases in HEAs.[18] It is understood that a Ni-based superalloy, where γ-FCC matrix coexists with the cuboidal γ'- ($L1_2$) precipitates, is the best example to have interesting properties, *i.e.*, high strength at elevated temperature due its stable major two-phase microstructure. Similar to the special class of alloys, HEAs are also reported to have a good combination of properties due to the formation of B2 and $L1_2$ phases within the BCC and FCC matrices.[18] The B2 phase is an ordered structure based on BCC (Pearson symbol cP2), wherein the body-centered position is occupied by one type of atom and corners are occupied by another kind of atom. The most common compounds that have this structure are CsCl and NiAl. An alloy with a high content of $L1_2$ for strengthening was designed by increasing the Ni content rather than reducing the Al content in the $Al_{0.5}Cr_{0.9}FeNi_{2.5}V_{0.2}$ alloy composition. Vanadium was added to strengthen and stabilize the $L1_2$ phase in the disordered FCC matrix. This composition is reported to have the highest tensile strength of 1.9 GPa among all the reported HEAs along with good ductility.[20] Formation of the B2 phase has been observed in many equiatomic or non-equiatomic HEAs as a major or minor phase.[21] Ma *et al.*[22] reported the formation of cuboidal nanoprecipitates in BCC HEAs based on the $Al_2(NiCoFeCr)_{14}$ composition and determined the factors affecting the formation of the B2 precipitates. The effect of these precipitates on the mechanical properties was discussed to understand the operating strengthening mechanisms in these alloys. In some cases, the formation of the B2 phase was reported during heat treatment of HEAs.[23,24] Moreover, it was observed that the alloys containing Fe, Co and Ni along with Al showed a strong affinity to forming B2 phase. Formation of the B2 phase along with Fe-Cr-rich disordered BCC phase has been observed more frequently in the AlCrFeCoNi HEA system.[8,25] It is well understood that by varying the concentration of Al in $Al_xCoCrFeNi$ HEA, different microstructures can be developed from FCC ($x \leq 0.45$) to BCC and then B2 ($x \geq 0.88$). Hao *et al.*[26] reported the formation of coherent cuboidal B2 nanoprecipitates in BCC matrix $Al_{0.7}NiCoFe_{1.5}Cr_{1.5}$ HEA. Adopting the various heat-treatment schedules, they found that the cuboidal B2 precipitate is stable with little or no coarsening at 773 K for 1080 hour. Formation of Fe-Cr-rich σ phase along with the FCC phase is reported when heat treatment is done above 873 K, making the alloy more brittle. Meng *et al.*[27] have studied the effect of Cr addition on the microstructure, room temperature flow and fracture behavior of as-cast $Fe_{30}Ni_{20}Mn_{35}Al_{15}$ alloy. A two-phase microstructure of B2 (Ni-Al-rich) and Fe-Mn-rich FCC phase is observed for Cr ≤ 6 at. pct, while on increasing the Cr content a more complex microstructure evolves The room temperature elongation to failure increases with increasing the Cr content (6 at. pct) compared to Cr free alloy. However, subsequently it decreases after a certain amount. Considering the advantages of precipitation hardening in HEAs and also other strengthening mechanisms compared to that of single phase HEA matrix, He *et al.*[28] have investigated the effect of nanosized coherent precipitates such as $L1_2$-Ni_3(Al-Ti) in a FeCoNiCr HEA FCC matrix with minor addition of Al and Ti. Extraordinary tensile properties were achieved through thermo-mechanical processing and microstructure controlling. Several alloys have been designed by varying the compositions to modify the microstructure as per the requirements.[29] These aspects of designing HEAs have shifted the focus toward developing new HEAs with more emphasis on the applications of these alloys.

In view of exploring the possibilities of designing precipitation-strengthened HEAs through microstructural tailoring by exploiting their stability and complex phase transformation behavior, the present investigation is aimed at developing the precipitation-hardened iron-rich non-equiatomic $Fe_{40}Cr_{25}Ni_{15}Al_{15}Co_5$ medium-entropy alloy (MEA), which will be close to high-entropy steel in many aspects. Moreover, the effect of configurational entropy, which is lower than that of the equiatomic AlCoCrFeNi HEA, is also explored to determine its phase formation and stability.

II. MATERIALS AND EXPERIMENTAL DETAILS

Alloys of Fe-C, Fe-Cr and elemental metals of Ni, Al and Co with purity ≥ 99.99 pct were used as the starting materials. Pieces were cut and mixed in an appropriate proportion to achieve the composition of $Fe_{40}Cr_{25}Ni_{15}Al_{15}Co_5$ for induction melting (IM). The composition has been expressed in atomic percent and weight percent (see Table I). A 1.5 kg mixture of the above composition was melted in the MgO crucible at ~ 1700 °C (1973 K) and was kept at this temperature for 20 minute to ascertain better chemical homogeneity. The molten alloy was poured into the copper mold of 150 mm × 100 mm × 15 mm dimensions and was allowed to solidify in air. Samples were cut from the slab for further investigations in the as-cast and heat-treated conditions. Samples were then heat treated at 873 K and 1173 K for 2 hour followed by water quenching. In another case, samples were kept at 873 K, 1173 K for 2 hour and 1073 K for 12 hour followed by furnace cooling (Figure 9). The crystalline phases in the as-cast and heat-treated alloys were characterized by XRD [Rigaku Mini flex-600 (40 kV to 15 mA)] with Cu-Kα radiation (λ = 0.154 nm) and with high-resolution XRD techniques [PANalytical EMPYREAN (40 kV to 40 mA)] with Co-Kα radiation (λ = 0.179 nm). The microstructure characterization was done by optical microscopy (Metalux-3), scanning electron microscopy (SEM) (FEI Quanta 200F) operating at 20 kV and transmission electron microscopy (TEM TECHNAI G2 T20) operated at 200 kV. The optical and the SEM samples were prepared by conventional metallographic polishing and etching. The TEM samples were prepared by a twin-jet electro-polisher in a solution of 90 pct CH_3OH and 10 pct $HClO_4$ (volume fraction) at the cryogenic temperature of 253 K. Thermal analysis of the as-cast sample was performed by using the NETZSCH DSC 404F apparatus in a nitrogen atmosphere at a constant

Table I. Expression of Atomic Percentage Into Weight Percentage Used in $Fe_{40}Cr_{25}Ni_{15}Al_{15}Co_5$ MEA

Elements	Fe	Cr	Ni	Al	Co
Atomic (Pct)	40	25	15	15	5
Weight (Pct)	43.68	25.42	17.22	7.91	5.76

heating rate of 40 K/min. The Vickers microhardness tester was used to measure the hardness of the as-cast and heat-treated alloys. Hardness measurements were performed at different loads of 100, 300 and 500 g with a dwell time of 10 second for all conditions of the samples. At least ten measurements were taken for each load to verify the results. The cylindrical specimens of dimension Φ 6 $\times$ 10 mm were used for compression testing. The test was performed in the INSTRON universal testing machine (model: 5982, rating: 100 kN static) at room temperature with a crosshead speed of 0.50 mm/min.

III. RESULTS

The X-ray diffraction patterns of $Fe_{40}Cr_{25}Ni_{15}Al_{15}Co_5$ MEA in as-cast condition and after heat treatment at 873 K and 1173 K for 2 hour are displayed in Figure 1. The as-cast sample showed the formation of a two-phase structure of ordered B2 and BCC phase. The formation of the ordered phase is confirmed through the presence of the (100) superlattice diffraction peak. The average lattice parameters of B2 and BCC phases are 2.88 $\pm$ 0.02 and 2.87 $\pm$ 0.01 Å, respectively, in the as-cast condition. The relative intensity of the (100) peak of B2 phase is higher than that of the (110) peak of the B2 and BCC phase. This indicates that the B2 phase might be strongly oriented with respect to the BCC phase. The heat-treated sample at 873 K exhibits the similar phase constitution of B2 and BCC phase. The only noticeable change is the decrease in the intensity of the characteristic peak (100) of the B2 phase, along with the appearance of other peaks (211), (200). This is again probably due to the partial disordering of the B2 phase after heat treatment at this temperature. The (110) plane shows a higher intensity compared to that of the as-cast alloy. This infers that the volume fraction of the BCC phase has increased after heat treatment at 873 K. On further increase in heat treatment temperature at 1173 K, no change in phase constituents was observed.

The microstructural evolutions of the as-cast and heat-treated samples were investigated by optical microscopy. Figure 2 depicts the optical micrographs of the as-cast sample and the heat-treated samples at 873 K and 1173 K for 2 hour followed by water quenching. As-cast alloy exhibits the formation of a columnar/dendritic microstructure (Figure 2(a)). The width of columns/dendrites varies in the range of 50 to 100 μm in the as-cast state. It has been observed that the heat-treated samples retained the columnar/dendritic

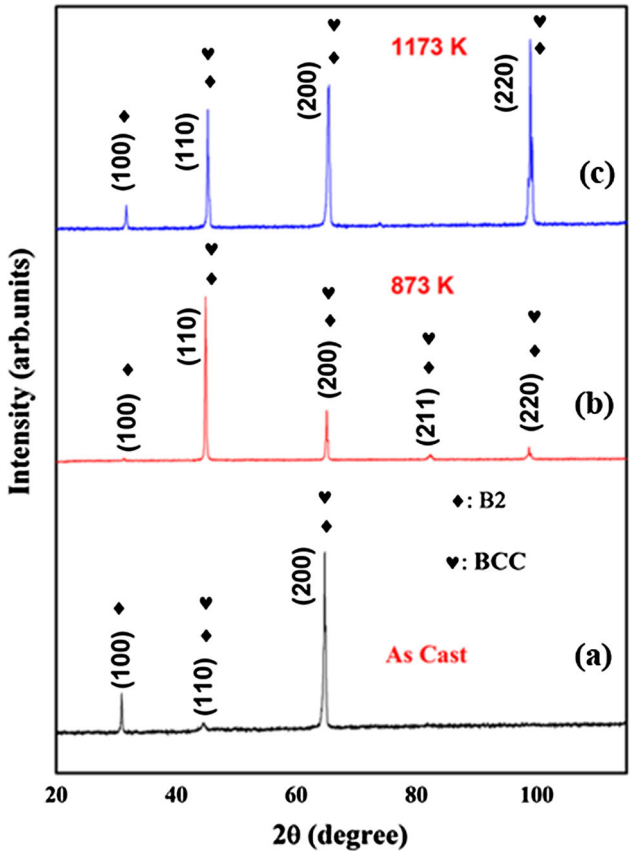

Fig. 1—X-ray diffraction patterns of $Fe_{40}Cr_{25}Ni_{15}Al_{15}Co_5$ MEA in (*a*) as-cast condition and after heat-treatment at (*b*) 873 K and (*c*) at 1173 K for 2 h, followed by water quenching. Evolution of the two-phase structure of (B2 + BCC) could be discerned.

structure even at 873 K and 1173 K, respectively. However, the change in the size of columnar grains/dendrites could be observed as the temperature increased.

The chemical compositions of the constituent microstructural features were analyzed using SEM-EDS full-frame analysis, and the results are listed in Table II. The experimental results are justifiable in relation to the initial compositions of the as-melted alloy. To examine the two-phase nature of the BCC/B2 matrix, transmission electron microscopy (TEM) analysis was performed. The bright-field image and the corresponding selected area diffraction (SAD) pattern of the as-cast alloy are shown in Figure 3.

The bright-field image (Figure 3(a)) showed that the cuboidal B2 precipitates are uniformly distributed in the BCC matrix. These cuboidal B2 precipitates of sizes ranging from 100 to 200 nm are embedded within the disordered BCC matrix. In the diffraction pattern (Figure 3(b)), a cubic pattern with a fourfold rotation symmetry is easily noticed. Additionally, a modulation of intensity among the diffraction spots is identified, which may be due to the partial or complete ordering of either the B2/BCC phase or both phases simultaneously. Whatever the situation, there is a strong orientation relationship between the two phases. The orientation relationship, *i.e.*, [100] of B2 phase, is parallel to the [100] of BCC phase, and the [110] of the B2 phase is

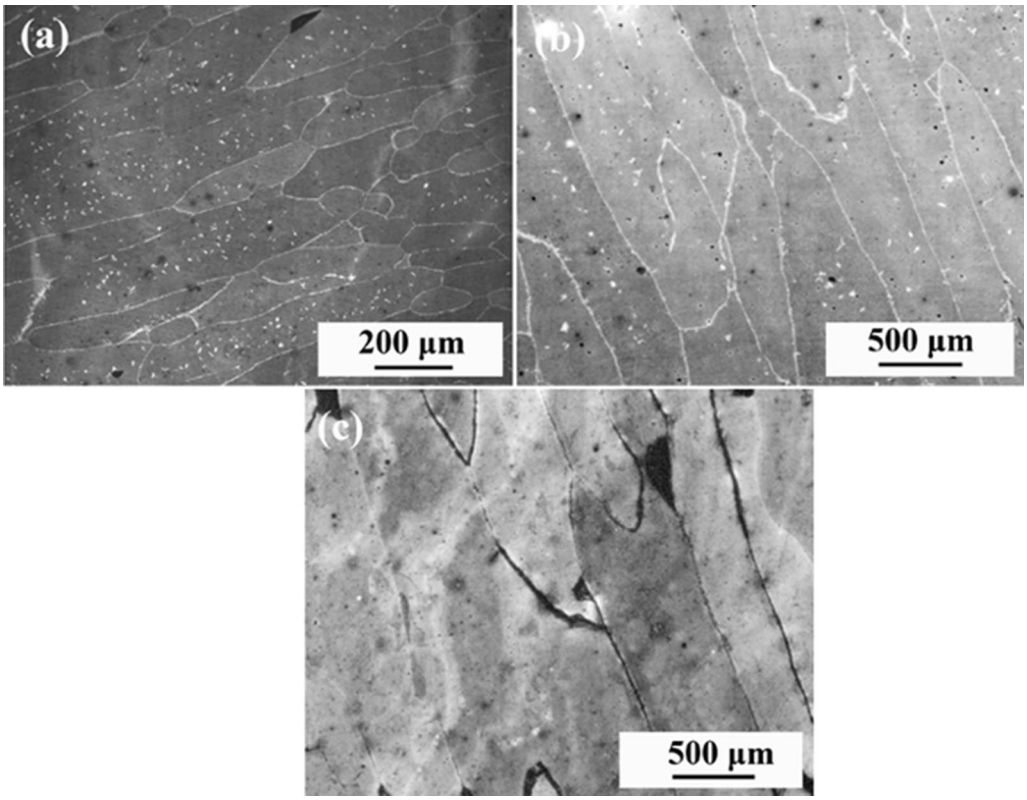

Fig. 2—Optical micrographs of $Fe_{40}Cr_{25}Ni_{15}Al_{15}Co_5$ medium-entropy alloy (*a*) as cast and after heat treatment at (*b*) 873 K and (*c*) 1173 K for 2 h followed by water quenching. Columnar grains/dendrites could be observed in all micrographs.

parallel to the [110] of BCC phase. This is commonly known as the cube-on-cube orientation relationship with no in-plane rotation. In this situation, the interface between the cuboid and the matrix is likely to be (100) type. A closer view of the B2 precipitates with the BCC matrix can be seen in the magnified image (Figure 3(c)). Figures 3(c) and (d) shows the bright- and dark-field imaging of the B2 precipitate with the matrix. Presence of the dislocation lines could be observed in the B2 phase and in the BCC matrix in the bright- as well as dark-field image [generated from (100) reflection]. The appearance of the dislocation lines indicates that they are most likely of mixed type. The presence of the thickness fringes at the interface of the cuboids further confirms the polyhedral nature of the precipitates. While some of the dislocations end at the BCC-B2 interface, some dislocation do cross over the interface. This is probably due to the semi-coherent nature of the interface. The elemental distribution with compositional information of the as-cast HEA was analyzed through STEM-EDS mapping (Figure 4). It has been found that Fe and Cr are richer in the matrix, and the cuboidal precipitates are enriched in Al and Ni. Cobalt (Co) appears to be distributed across the precipitates and the matrix; however, it is richer in matrix. It further helps in substantiating the fact that the matrix is rich in Fe and Cr and of BCC structure, whereas the precipitates are more likely Al-Ni-rich B2-type ordered phase. Co is present in the BCC matrix and in the B2 cuboidal phase. Even though the B2 phase appears to be ordered, some amount of Co has ingressed into it, and it probably has substituted the Ni site in the lattice leading to a partially ordered structure. This observation points toward a solute rejection mechanism of B2 phase nucleation in the BCC matrix. While at nucleation stage, Fe and Cr are rejected by the cuboidal precipitates, leading to the enrichment of Fe and Cr in the BCC matrix.

Figure 5 shows a similar behavior of compositional variation of cuboidal B2 precipitates that are enriched in Ni and Al elements, and the matrix is rich in Fe and Cr. To understand the thermal stability of the alloy, differential scanning calorimetry (DSC) was conducted on the as-cast alloy.

The DSC thermogram of the as-cast $Fe_{40}Cr_{25}Ni_{15}Al_{15}Co_5$ MEA is given in Figure 6. No major heat evolution event was seen to occur in the alloy. However, an indication of the exothermic event, which ranges from 400 °C to 600 °C (673 K to 873 K), could be observed. This might indicate the increase in the structural order or solute redistribution, which are essentially diffusion-dominated processes.

To further substantiate this exothermic event, heat treatment of the alloy was conducted at 873 K and 1173 K for 2 hour and at 1073 K for a longer holding time of 12 hour followed by furnace cooling. The X-ray diffraction patterns of the heat-treated samples along with as-cast alloy are given in Figure 7. At 873 K, there is no change in the phase that could be observed except

Table II. The Chemical Composition of the Constituent Elements in As-Cast $Fe_{40}Cr_{25}Ni_{15}Al_{15}Co_5$ MEA

Elements	Fe-K	Cr-K	Ni-K	Al-K	Co-K
Atomic Pct (Calculated)	40	25	15	15	5
Atomic Pct (Experimental) Error (± 5 Pct)	40.7	26.8	13.3	14.8	4.5

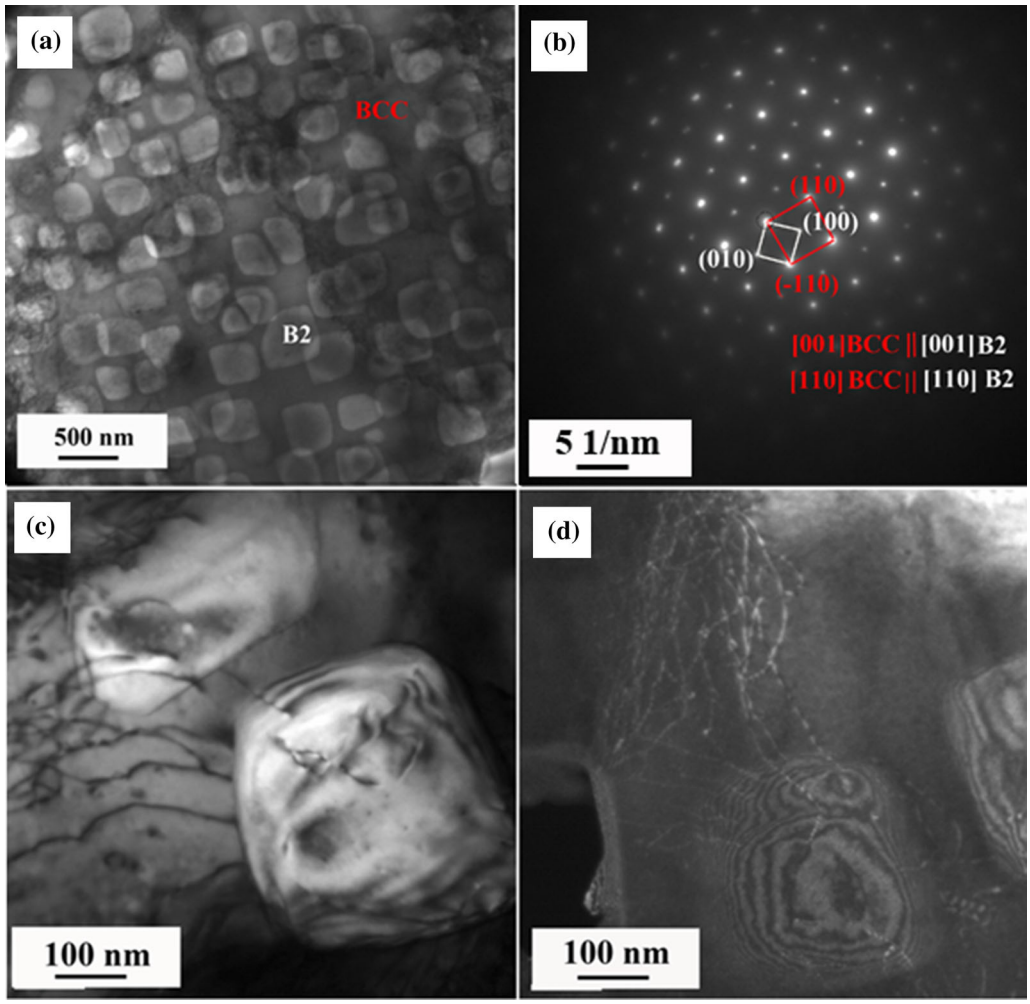

Fig. 3—(*a*) Bright-field electron micrograph and (*b*) selected area diffraction pattern (SAD) of as-cast $Fe_{40}Cr_{25}Ni_{15}Al_{15}Co_5$ MEA. Cuboidal B2 precipitates are embedded in the BCC disordered matrix. (*c*) and (*d*) bright- and dark-field images of B2 precipitates within the disordered BCC matrix. (100) reflection was taken into account to collect the dark-field image.

the increase in intensities of the peaks. This may happen because of the release of the crystal strain during the heat treatment of the alloy. Further increase in heating temperature at 1173 K shows the increase in the intensity of the first superlattice reflection (100) of the B2 phase relative to the as-cast structure. This suggests that with the increase in heat treatment temperature, the degree of ordering increases. A strong orientational order and/or cut surface of the sample also might affect such intensity variation. This means the volume fraction of the B2 phase increases. Long-term thermal stability of the evolved phases in the as-cast alloy was further investigated at a longer holding time of 12 hour at 800 °C (1073 K).

No sign of phase transformation could be observed even at a longer holding time. The diffraction pattern after heat treatment at this temperature showed all the reflections of the B2 phase. Therefore, it is imperative to say that the B2 type ordered phase is stable over a higher time-temperature range. To understand the phase stability at higher temperature with longer holding time, the sample was heat treated at 900 °C (1173 K) for 24 hour followed by water quenching. The corresponding X-ray diffraction pattern and optical micrograph are given in Figure 8.

The phase morphology, as observed from the optical micrograph, remains the same, and the nature of the XRD pattern also remains qualitatively the same.

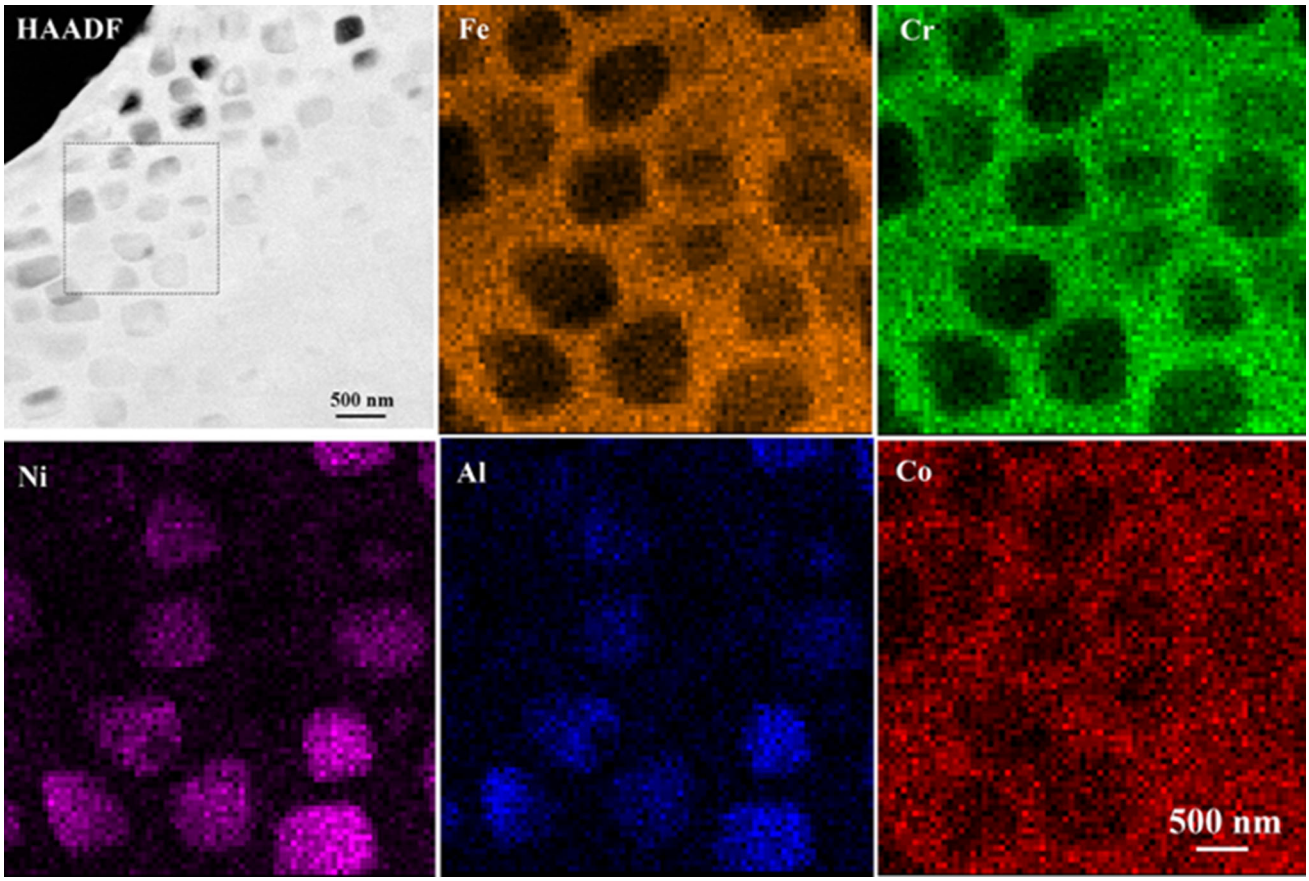

Fig. 4—STEM-EDS mapping of as-cast $Fe_{40}Cr_{25}Ni_{15}Al_{15}Co_5$ medium-entropy alloy. Cuboidal B2 precipitates are richer in Ni-Al, and the BCC matrix is mostly of Fe-Cr elements. Co is homogeneously distributed in the alloy.

However, detailed observation and analysis showed that in the XRD pattern shouldering/splitting is present with the principal reflections. Enlarged views of the principal reflections are given in Figures 8(c) and (d), respectively. In the (100) superlattice reflection, no shouldering or splitting is observed except minimal broadening. This indicates that the ordered phase is still quite fine in size and no new ordered phase has evolved during the high-temperature heat treatment. However, in (110) and (200) reflections, extensive shouldering/splitting can be observed. When deconvoluted, the (110) and the (200) peaks can be resolved into several closely spaced reflections. Detailed analysis of the deconvoluted peak positions is given in Table III. In the table, corresponding to each experimental and deconvoluted peak position and corresponding to other possible peak positions, the lattice parameter has been calculated. The experimental and calculated d-spacings and the calculated lattice parameters are approximated after the second place of the decimal as in XRD getting accuracy beyond the second place of the decimal is not reliable. As mentioned earlier, the (100) superlattice reflection corresponding to the ordered B2 phase cannot be deconvoluted into more than one peak. Based on the experimental value of the (100) peak, the corresponding (110) and (200) interplanar distances have been calculated as 2.02 and 1.43 Å respectively for the (110) and (200) peaks. Interestingly, 2.02 and 1.43 Å appear as the experimental values in one of the deconvoluted peaks in the subsequent sections of the table. This confirms that the ordered B2 phase is still present with lattice parameter 2.85 Å, which is less than the lattice parameter of the B2 phase in the as-cast alloy. Experimentally observed and deconvoluted peak positions for the (110) peak are given in the next section of the table. They are quite close to one another. In the usual manner, the deconvoluted (110) peak positions have been used to calculate the peak positions of (200) and (100) peaks. Almost all the experimental (200) peak positions are matched in this case also. However, only one (100) peak is present. When the same exercise is repeated for the (200) experimental peak, other peaks can also be regenerated. It can be summarized from this XRD pattern that there is one ordered B2 phase with the lattice parameter of 2.85 Å. However, around the (110) peak of the B2 phase small shoulder peaks can be observed for which (100) superlattice reflection cannot be observed. This indicates that a certain volume fraction of disordered B2 phase is also present after the heat treatment. It might be understood that the preexisting ordered B2 phase had undergone disordering transformation while the heat treatment or new disordered B2 phase had freshly nucleated during the heat treatment. However, the ordered B2 phase after heat

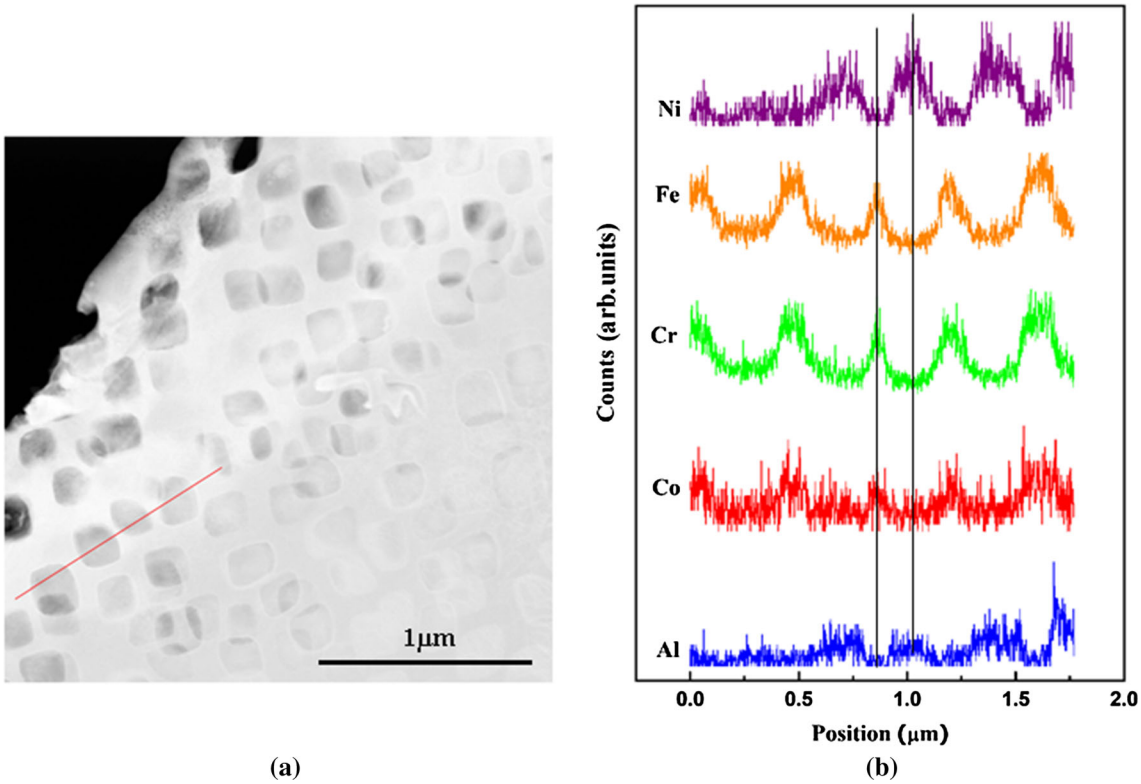

Fig. 5—(*a*) HAADF image showing the line area for composition analysis; (*b*) corresponding profile analysis of each element in as-cast $Fe_{40}Cr_{25}Ni_{15}Al_{15}Co_5$ medium-entropy alloy. Two vertical lines showing the clear distribution of Fe-Cr- and Al- Ni-rich elements.

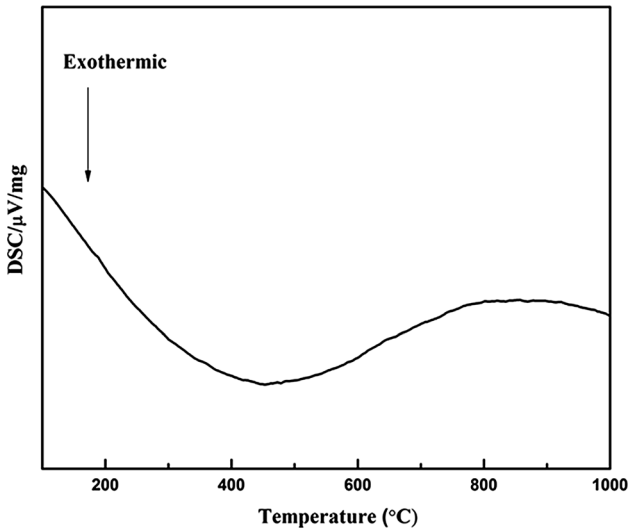

Fig. 6—Differential scanning calorimetric (DSC) thermogram of as-cast $Fe_{40}Cr_{25}Ni_{15}Al_{15}Co_5$ MEA. No major heat event is observed. A wide exothermic peak over a range of temperature is attributing to strain relaxation.

treatment has a smaller lattice parameter than the ordered B2 phase after casting. This can be attributed to solute rearrangement in the ordered B2 phase during heat treatment. The disordered B2 phase might have a marginally higher lattice parameter than the ordered ones. This observation mostly supports the idea of solute rearrangement during heat treatment. In a similar line, three very closely related lattice parameters could also be observed for the BCC phase. All the lattice parameters are marginally lower than the as-cast lattice parameter. This again points toward the solute rearrangement mechanism operating during heat treatment. More importantly, though, this alloy has two basic phases, *i.e.*, B2 and BCC, but it has six polymorphically related phases. Existence of such polymorphically related phases and the thermodynamic and functional implications will be discussed later. It should be pointed out that the relative area under the deconvoluted peak positions should not be used to assess the volume fraction of these different phases. Even though the multiplicity factor and temperature factors can be calculated with relative ease, the calculation of the structure factor could be very incorrect as the right composition and site occupancy in the structures of these phases are not known.

The mechanical behavior of the as-cast and heat-treated samples of $Fe_{40}Cr_{25}Ni_{15}Al_{15}Co_5$ MEA at 600°C and 900 °C was investigated by performing the room temperature compression test. The obtained graphs of the engineering stress (MPa) and plastic strain are depicted in Figure 9, and the values are listed in Table IV. The alloy is found to have the yield strength (0.2 pct offset) of ~ 1047 MPa and ultimate strength of ~ 1133 MPa. The yield strength of the studied alloy is comparable to that of the earlier reported HEAs, but the alloy lacks in plasticity.

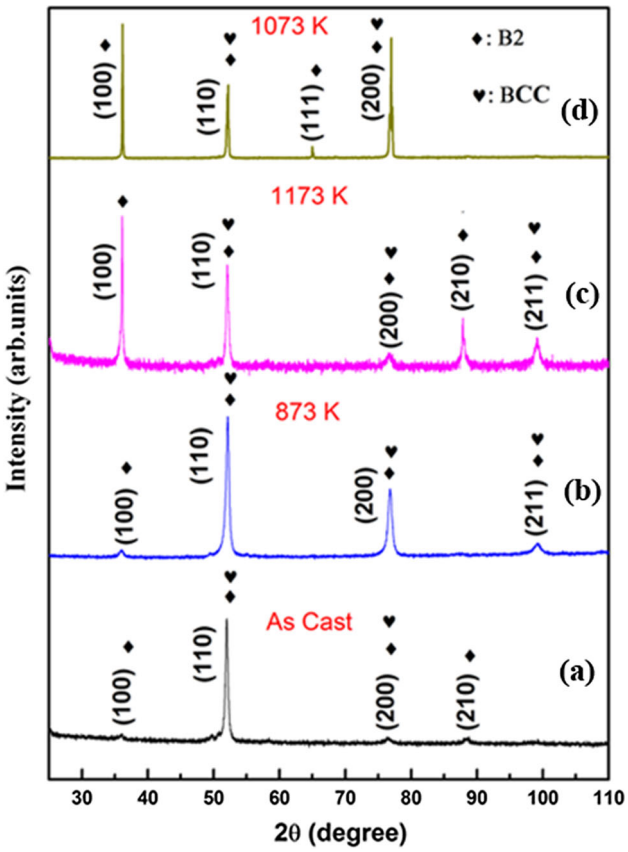

Fig. 7—X-ray diffraction patterns of (*a*) as-cast and (*b*) and (*c*) heat-treated samples at 873 K and 1173 K for 2 h, respectively, and (*d*) heat-treated at 1073 K for 12 h and cooled down in a furnace. Evolution of similar types of phase could be observed in all conditions.

This might have resulted from the presence of the brittle Ni-Al-based B2 type intermetallic phase. However, the heat-treated sample at 600 °C (873 K) showed an increase in yield strength (~ 1306) and ultimate strength (~ 1590 MPa) with a significant increase in plasticity. This is due to the increase in the volume fraction of B2 phase with the softening of the matrix phase. With a further increase in temperature [900 °C (1173 K)] the similar trend followed of an increase in yield strength (~ 1320 MPa) and ultimate strength (~ 1709 MPa). This is due to the increase of the volume fraction of B2 phase with the annealing temperature. The microhardness measurements were performed for the as-cast and heat-treated samples (water quenched) to evaluate the hardness of the alloy. The observed results for 100 g load are listed in Table IV. The hardness values increase with an increase in the annealing temperature, *i.e.*, from ~ 391 to ~ 423 HV.

IV. DISCUSSION

The evolution of the phases, thermal stability and mechanical behavior of the presently investigated alloy can be understood in more detail in the following sections.

A. *Phase Evolution in As-Cast $Fe_{40}Cr_{25}Ni_{15}Al_{15}Co_5$ MEA*

The as-cast structure of the $Fe_{40}Cr_{25}Ni_{15}Al_{15}Co_5$ MEA showed the formation of BCC-derived B2-type intermetallic phase enriched in Ni-Al composition. The formation of Ni-Al-rich B2-type phase in Fe-Cr-rich matrix can be better understood from the thermodynamic point of view. For this purpose, the mixing enthalpies (ΔH_{mix}) of the binary components in the alloy were calculated using the Miedema model[30] and are given in Table V. The mixing enthalpy of the Ni-Al pair is more negative (− 22 kJ/mol) compared to that of the other pairs. Therefore, this alloy favors the formation of Ni-Al-rich ordered phase. The Ni-Al-rich particles are thought to be formed during cooling of the compositionally rich Fe-Cr matrix. The limited solid solubility of the Ni-Al leads to formation of Ni-Al-rich particles in the Fe-Cr-rich BCC matrix. Apart from the above-mentioned mixing enthalpy factor, the valence electron concentration (VEC) is also reported to affect the structural evolution.[31] The valence electron concentration for multicomponent alloy is calculated as:

$$\mathrm{VEC} = \sum_{i=1}^{n} c_i(\mathrm{VEC})_i \qquad [1]$$

where c_i is the atomic concentration and $(\mathrm{VEC})_i$ is the ith element. The VEC for the present alloy is 7.1. It is established that when VEC is ≥ 8, it favors the formation of the FCC type of solid solution, but if it is ≤ 6.87, it prefers the formation of BCC-type solid solution while intermediate values support the formation of mixed structures. The calculated value of the present MEA lies in the intermediate range of BCC and FCC. Thus, the VEC criterion does not hold for the present alloy to predict the structural evolution. As we mentioned earlier, the present alloy was designed to determine the role of configurational entropy in phase formation by deviating the typical range of equiatomic elemental concentration. The investigated alloy showed evolution of the two-phase structure (B2 + BCC), implying that the role of configurational entropy may be an important factor in the formation of simple solid solution phases. However, the formation of phases is basically governed by binary atomic paring between constituent elements and the competition of entropy and enthalpy for minimizing the Gibbs free energy. All the potential thermodynamic and physical parameters of the present alloy are calculated and displayed in Table VI. Mixing the enthalpy and atomic size difference (δ) of the alloy is also a favorable condition for forming solid solution phases. Yao *et al.*[32] have designed non-equiatomic $Fe_{40}Mn_{27}Ni_{26}Co_5Cr_2$ HEA and reported the formation of a stable single phase of FCC structure. This alloy composition ruled out the necessary criteria for achieving a single-phase solid solution in HEAs. Additionally, Ghosh *et al.*[33] have shown that the competition between the chemical and elastic component of enthalpy plays an important role in determining whether or not a single-phase solid solution may be formed. Even if the chemical enthalpy is negative and favorable, the second component is

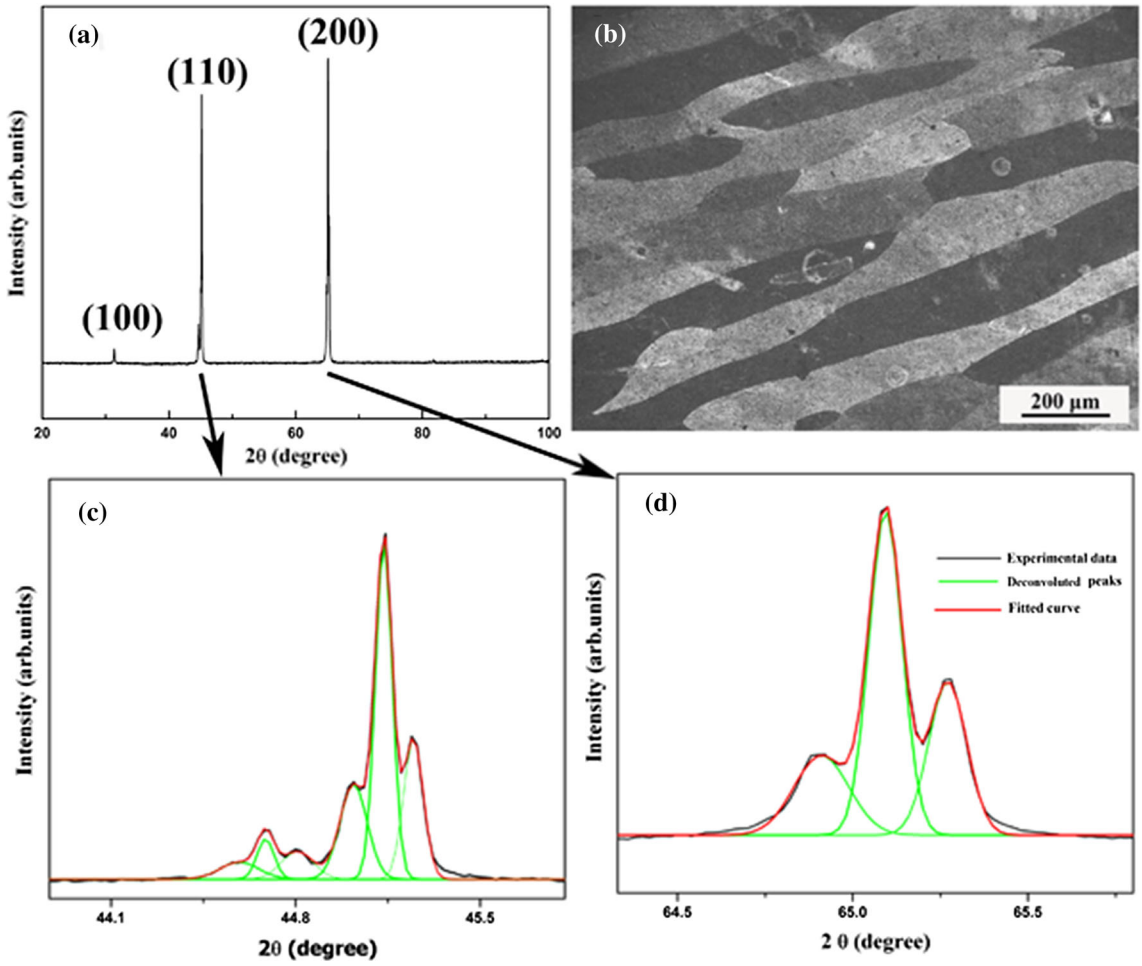

Fig. 8—X-ray diffraction pattern of (*a*) heat-treated sample at 1173 K for 24 h and then water quenched (*b*) corresponding the optical micrograph of same sample; (*c*) and (*d*) enlarged view of the two intense peaks, deconvoluted to show the distinct peaks.

introduced into the solution, which increases the elastic strain steadily. Eventually, it destabilizes the single solid solution phase. Formation of the equilibrium shape of any precipitates is basically governed by minimizing the total energy of the state. This includes the elastic and interfacial energy of a system.[34,35] When the sizes of the precipitates are small, the elastic strain energy induced by the lattice mismatch of the precipitate and matrix is less. In that case, the shape of the precipitate is primarily controlled by minimizing the surface area, which will lead to formation of the spheroidal or ellipsoidal shapes of particles. However, when the precipitates start growing, the elastic strain energy becomes dominant, and the relative contribution of both energies to the total energy can be quantified by using the characteristic parameter (L) (10^{-1}).[26] This L parameter is used to represent the energy state of a precipitate at equilibrium

$$L = \frac{\varepsilon^2 C_{44} r}{s} \qquad [2]$$

where ε is the lattice misfit strain, C_{44} is the elastic constant for the matrix, r is the average precipitate size, and s is the average specific interfacial energy. For the present alloy, the lattice misfit strain (ε) between the BCC and B2 phase is calculated by using the equation of $\varepsilon = 2 \times (a_{B2}\text{-}a_{BCC})/(a_{B2} + a_{BCC})$, where a_{B2} and a_{BCC} are the lattice parameters of B2 and BCC phase. The ε and r values for the present alloy are 0.138 pct and ~ 300 ± 20 nm, respectively. C_{44} and s values for the BCC/B2 are taken from the B2-NiAl phase, being 130 GPa and 0.125 J/m^2, respectively. The moderate value of L (0.59) for the present alloy favors the formation of coherent cuboidal B2 precipitates. These results were correlated with (Al, Sc)-based alloys where the coherent precipitates of Al_3Sc ($L1_2$) in aluminum alloys change from spheres to cuboids and then plates as the size of the precipitate increases.[30]

B. *Thermal Stability of $Fe_{40}Cr_{25}Ni_{15}Al_{15}Co_5$ MEA*

The dynamic differential scanning calorimetric (DSC) thermogram of as-cast $Fe_{40}Cr_{25}Ni_{15}Al_{15}Co_5$ MEA showed no major phase transformation event. The minor exothermic event in the temperature range of 400 °C to 600 °C (673 K to 873 K) was observed. This exothermic event was substantiated by following the annealing treatments at 873 K and 1173 K for 2 hour.

There was no sign of phase transformation during this thermal treatment. Only noticeable change in intensity of the superlattice refection peaks was observed. This might be due to the increase of the volume fraction of the ordered phase. In the same line, the alloy was further annealed at 1073 K for 12 hour. The alloy was found to be thermally stable even at a longer holding time. It was further substantiated by heat treatment at 1173 K for a longer holding time of 24 hour. High thermal stability is the result of the formation of the precipitation hardening with stronger bonding between unlike pairs of Ni-Al atoms and slower diffusion kinetics (due to the presence of multicomponent elements).[36] Lack of phase diagram data in higher order alloy systems is one of the impending problems related to understanding the phase stability in multicomponent alloys. It has been already pointed out for multicomponent bulk metallic glass forming alloys,[37] and this concept holds equally well for multicomponent high-entropy or medium-entropy alloys. It is moreover emphasized that in multicomponent alloys the potential energy landscape could be a shallow megabasin with several local minima. During processing and subsequent heat treatment the alloy may get held up in a local minima and may continue to hop to several such local minima. Basu and Ranganathan[38–40] previously showed for glass forming alloys that while precipitating stable or metastable crystalline or quasicrystalline phases the remaining matrix may also experience a gradual compositional shift and the final microstructure may not be thermodynamically stable, though it could be kinetically stabilized. In the present study also a similar behavior is observed. In the DSC thermogram, no sharp transformation event is observed, even though it spans over a large range of temperature. During heat treatment also no phase change is observed. However, after long-term heat treatment a reduction in the lattice parameter in BCC and the B2 phase is observed, which may be related to the compositional repartitioning or strain energy minimization in the phases as well as at the interfaces. Further proof is obtained by detailed analysis of the XRD after long-term heat treatment when shouldering or splitting in the major diffraction peaks could be observed. These broadened peaks can be deconvoluted to a few more polymorphically related BCC or B2 phases. It can be inferred from this observation that during this long-term heat treatment, compositional partitioning within the phases takes place, which results in reduction in the lattice parameter, readjustment of the bulk and interfacial strain as well. This also explains why the exothermic event in DSC appears over a long temperature range. Moreover, this alloy also shows the hopping behavior that has been observed in multicomponent glass forming alloys.

C. *Mechanical Properties of $Fe_{40}Cr_{25}Ni_{15}Al_{15}Co_5$ MEA*

The present alloy in as-cast condition showed the yield strength of ~ 1047 MPa and ultimate compressive strength of ~ 1133 MPa, comparable to that of the reported HEAs. However, the alloy showed the limited values of uniform compressive strain (3 pct) and total compressive strain (5 pct) in as-cast state because of the formation of the intermetallic phase B2 in the BCC matrix. The heat-treated sample exhibits an increase in yield strength and compressive strain (see Table IV) due to the increase of the volume fraction of B2 phase and softening of the matrix phase. Furthermore, an increase in heat treatment temperature [900 °C (1173 K)] followed a similar trend of increase in yield strength and elongation. Similar observations of increase in hardness with annealing temperatures were made for the alloy. Zhou *et al.*[41] have reported the hierarchical nanostructured $Fe_{34}Cr_{34}Ni_{14}Al_{14}Co_4$ HEA with a good combination of high strength (yield strength 1353 MPa and fracture strength 2638 MPa) and large plasticity (40.6 pct). The strengthening mechanisms in polycrystalline materials are traditionally governed by four methods: solid solution hardening associated with point defects in the crystal, grain boundary hardening with planar defects in the crystal, dislocation hardening associated with line defects and precipitation/dispersion hardening associated with volumetric defects in the crystal. In the present alloy, as the formation of precipitation of secondary particles was observed, it is believed that the excellent mechanical properties of the $Fe_{40}Cr_{25}Ni_{15}Al_{15}Co_5$ MEA are mostly attributed to the second-phase strengthening mechanism. The formation of coherent B2 precipitates in the BCC matrix has a similar strengthening mechanism of Ni-base superalloys. In Ni-base superalloys, the cuboidal gamma prime precipitates with $L1_2$ structure (Cu_3Au-type) embedded coherently with a FCC gamma matrix. The formation of second-phase particles has been widely used as a strengthening mechanism for structural applications. Second-phase particles are expected to produce hardening, either through the dislocation bypass mechanism (Orowan type) or particle shearing mechanism. In general, the Orowan mechanism is valid when the size of the precipitates reaches a critical value or it is incoherent with the matrix. However, the shearing mechanism would operate when precipitates are sufficiently small and coherent. Based on the present precipitate morphology, the particle shearing mechanism is expected to dominate the strengthening mechanism. High hardness values of the HEAs are attributed to the lattice distortion effect, which arises because of the atomic size difference, crystal structure and bonding energy among constituent elements. $Fe_{40}Cr_{25}Ni_{15}Al_{15}Co_5$ being a MEA is strengthened mainly by the precipitation hardening of B2 precipitates where the yield strength of the material is > 1000 MPa and the ultimate compressive strength is > 1100 MPa. It is known that the high entropy Cr, Ni-based alloys have generally shown good corrosion resistance, especially in H_2SO_4 and NaCl solutions, very good oxidation resistance and high thermal stability at > 800 °C. Therefore, future research should focus on the application of these medium entropy alloys for designing thinner gauge high-strength pipeline materials for the oil and gas industries.

Table III. List of Detailed Analysis of Deconvoluted Peaks of Heat-Treated Sample at 1173 K for 24 h and Then Water Quenched and Calculation of Lattice Parameter

Lattice Parameter of the BCC and B2 Phase in the As-Cast Material Lattice Parameter of the BCC Phase: $a = 2.87 \pm 0.01$ Å Lattice Parameter of the B2 Phase: $a = 2.88 \pm 0.02$ Å				
Heat-Treated Sample 1173 K for 24 h and Then Water Quenched Analysis of the 100 Peak in the XRD Pattern of the Sample Calculated Values are Approximated to Second Place of the Decimal				
2θ (Degree)	d(100) Å (Experimental)	d(110) Å (Calculated)	d(200) Å (Calculated)	Lattice Parameter (Å) (Calculated)
31.36	2.8509 to 2.85	2.0162 to 2.02	1.4255 to 1.43	2.8509 to 2.85
Analysis of (110) Peak in the XRD Pattern of the Sample Calculated Values are Approximated to Second Place of the Decimal				
2θ (degree)	d(100) Å (Calculated)	d(110) Å (Experimental)	d(200) Å (Calculated)	Lattice Parameter (Å) (Calculated)
44.5862	2.8702 to 2.87	2.029816 to 2.03	1.4351 to 1.44	2.8702 to 2.87
44.686	2.8641 to 2.86	2.025514 to 2.03	1.4321 to 1.43	2.8641 to 2.86
44.8066	2.8568 to 2.86	2.020342 to 2.02	1.4284 to 1.43	2.8568 to 2.86
45.0192	2.8440 to 2.84	2.011293 to 2.01	1.422 to 1.42	2.8440 to 2.84
45.1341	2.8371 to 2.84	2.00644 to 2.01	1.4186 to 1.42	2.8371 to 2.84
45.2464	2.8304 to 2.83	2.00172 to 2.00	1.4152 to 1.42	2.8304 to 2.83
Analysis of (200) Peak in the XRD Pattern of the Sample Calculated Values are Approximated to Second Place of the Decimal				
2θ (Degree)	d(100) Å (Calculated)	d(110) Å (Calculated)	d(200) Å (Experimental)	Lattice Parameter (Å) (Calculated)
64.9105	2.8697 to 2.87	2.0295 to 2.03	1.434852 to 1.43	2.8697 to 2.87
65.0938	2.8625 to 2.86	2.0244 to 2.02	1.431254 to 1.43	2.8625 to 2.86
65.2705	2.8556 to 2.86	2.0195 to 2.02	1.427806 to 1.43	2.8556 to 2.86

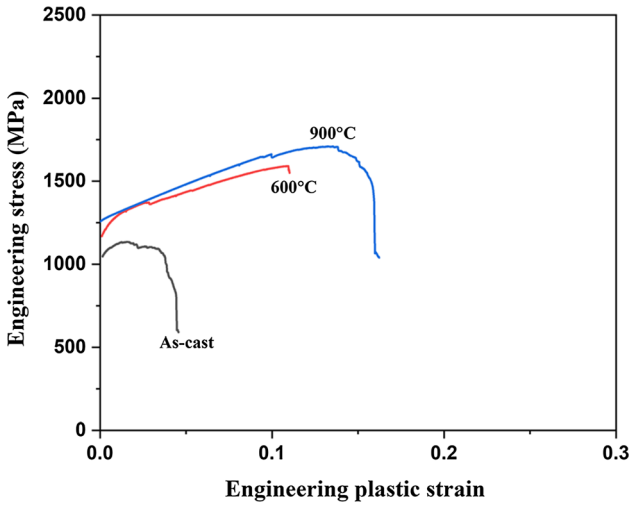

Fig. 9—Engineering stress-plastic strain curve obtained from the compression test of as-cast and heat-treated samples of $Fe_{40}Cr_{25}Ni_{15}Al_{15}Co_5$ MEA at room temperature.

V. CONCLUSIONS

The following conclusions can be drawn from the present investigation:

(i) A newly designed alloy composition of non-equiatomic $Fe_{40}Cr_{25}Ni_{15}Al_{15}Co_5$ MEA was developed successfully. The induction melting technique was found to be effective for producing the large quantity of this alloy composition.

(ii) Formation of the two-phase microstructure of Fe-Cr-rich BCC (2.87 ± 0.01 Å) and Ni-Al-rich ordered B2 (2.88 ± 0.02 Å) phase was observed in the as-cast condition. However, this alloy composition supports the prediction of the structures because of the valence electron concentration (VEC) for solid-solution formation in HEAs. The coexistence of these two phases has evolved perhaps because of solute rejection from a single-phase BCC structure.

(iii) The shape of coherent B2 precipitate was determined by lattice misfit ($\varepsilon = 0.138$ pct), which primarily governs the total energy (L) and is favorable for the formation of the cuboidal shape. The alloy had good structural stability at different heat treatment temperatures.

(iv) The BCC and B2 phases are quite stable at high temperature over a considerably long period of time. However, long exposure at high temperatures results in compositional repartitioning to reduce internal strain and the total energy of the system.

(v) The present alloy is found to have a good combination of high compression yield strength

Table IV. Compressive and Microhardness (HV) Results of $Fe_{40}Cr_{25}Ni_{15}Al_{15}Co_5$ MEA in As-Cast and Heat-Treated Samples

Sample Details	Yield Strength (Offset 0.2 Pct) (MPa)	Compressive Strength (MPa)	Uniform Compressive Strain (Pct)	Total Compressive Strain (Pct)	Vickers Microhardness (HV) Load: 100 g
As-Cast	1047	1133	3	5	391 ± 9
Heat Treated 600 °C (873 K) for 2 h	1306	1590	9	11	408 ± 5
Heat Treated 900 °C (1173 K) for 2 h	1320	1709	13	16	423 ± 8

Table V. The Calculated Values of Mixing Enthalpy (ΔH_{mix}(kJ/mol)) of Atomic Pairs for $Fe_{40}Cr_{25}Ni_{15}Al_{15}Co_5$ MEA by the Miedema Approach.[30]

Elements	Al	Co	Cr	Fe	Ni
Al	—	− 19	− 10	− 11	− 22
Co	− 19	—	− 4	− 1	0
Cr	− 10	− 4	—	− 1	− 7
Fe	− 11	− 1	− 1	—	− 2
Ni	− 22	0	− 7	− 2	—

Table VI. The Calculated Physical and Thermodynamic Parameters for $Fe_{40}Cr_{25}Ni_{15}Al_{15}Co_5$ MEA

Mixing Enthalpy (ΔH_{mix}) $\left(\frac{kJ}{mol}\right)$	Configurational Entropy (ΔS_{conf}) $\left(\frac{JK^{-1}}{mol}\right)$	Valence Electron Concentration (VEC)	Atomic Size Difference, Delta (δ) Pct
− 9.43	11.33	7.1	5.2

and hardness, *i.e.*, ~ 1047 MPa and 391 ± 5 HV, respectively, as well as reasonable ductility, which is mostly attributed to the precipitation strengthening effect. An increase in yield strength and plasticity was observed for heat-treated samples because of the increase in the volume fraction of B2 phase and softening of the matrix phase.

ACKNOWLEDGMENTS

The authors are thankful to Prof. R.K Mandal, Dr. Manish Kumar Singh, Yagnesh Shadangi and Priyatosh Pradhan for their help and stimulating discussion during the course of this work. The authors are also grateful to the Advanced Research Centre for Iron and Steel (ARCIS) of the Institute funded by the Steel Development Fund, Ministry of Steel, India, for providing melting and XRD facilities. The authors would also like to acknowledge the DST-FIST funding for providing the electron microscopy facility.

REFERENCES

1. J.W. Yeh, S.K. Chen, S.J. Lin, J.Y. Gan, T.S. Chin, T.T. Shun, C.H. Tsau, and S.Y. Chang: *Adv. Eng. Mater.*, 2004, vol. 6, pp. 299–303.
2. B. Cantor, I.T.H. Chang, P. Knight, and A.J.B. Vincent: *Mater. Sci. Eng. A*, 2004, vols. 375–377, pp. 213–18.
3. E.J. Pickering and N.G. Jones: *Int. Mater. Rev.*, 2016, vol. 61, pp. 183–202.
4. Y. Zhang, T. Ting, Z. Tang, M.C. Gao, K.A. Dahmen, P.K. Liaw, and Z. Ping: *Prog. Mater. Sci.*, 2014, vol. 61, pp. 1–93.
5. N.K. Mukhopadhyay: *Curr. Sci.*, 2015, vol. 109, pp. 665–67.
6. J.W. Yeh: *JOM*, 2013, vol. 65, pp. 1759–71.
7. V. Shivam, Y. Shadangi, J. Basu, and N.K. Mukhopadhyay: *J. Mater. Res.*, 2019, vol. 35, pp. 787–95.
8. W.-R. Wang, W.-L. Wang, S.-C. Wang, Y.-C. Tsai, C.-H. Lai, and J.-W. Yeh: *Intermetallics*, 2012, vol. 26, pp. 44–51.
9. M. Vaidya, G.M. Muralikrishna, and B.S. Murty: *J. Mater. Res.*, 2019, vol. 34, pp. 664–86.
10. T. Borkar, B. Gwalani, D. Choudhuri, C.V. Mikler, C.J. Yannetta, X. Chen, R.V. Ramanujan, M.J. Styles, M.A. Gibson, and R. Banerjee: *Acta Mater.*, 2016, vol. 116, pp. 63–76.
11. F. Otto, Y. Yang, H. Bei, and E.P. George: *Acta Mater.*, 2013, vol. 61, pp. 2628–38.
12. A.S. Sharma, S. Yadav, K. Biswas, and B. Basu: *Mater. Sci. Eng. R*, 2018, vol. 131, pp. 1–42.
13. M.H. Tsai and J.W. Yeh: *Mater. Res. Lett.*, 2014, vol. 2, pp. 107–23.
14. D.B. Miracle and O.N. Senkov: *Acta Mater.*, 2017, vol. 122, pp. 448–511.
15. C.Y. Hsu, T.S. Sheu, J.W. Yeh, and S.K. Chen: *Wear*, 2010, vol. 268, pp. 653–59.
16. S. Yadav, A. Kumar, and K. Biswas: *Mater. Chem. Phys.*, 2018, vol. 210, pp. 222–32.
17. S. Praveen, J. Basu, S. Kashyap, and R.S. Kottada: *J. Alloys Compd.*, 2016, vol. 662, pp. 361–67.
18. J. Chen, X. Zhou, W. Wang, B. Liu, Y. Lv, W. Yang, D. Xu, and Y. Liu: *J. Alloys Compd.*, 2018, vol. 760, pp. 15–30.
19. Y. Zou, J.M. Wheeler, H. Ma, P. Okle, and R. Spolenak: *Nano Lett.*, 2017, vol. 17, pp. 1569–74.
20. Y. Liang, L. Wang, Y. Wen, B. Cheng, Q. Wu, T. Cao, Q. Xiao, Y. Xue, G. Sha, Y. Wang, Y. Ren, X. Li, L. Wang, F. Wang, and H. Cai: *Nat. Commun.*, 2018, vol. 9, pp. 1–8.
21. D.G. Shaysultanov, G.A. Salishchev, Y.V. Ivanisenko, S.V. Zherebtsov, M.A. Tikhonovsky, and N.D. Stepanov: *J. Alloys Compd.*, 2017, vol. 705, pp. 756–63.
22. Y. Ma, Q. Wang, B.B. Jiang, C.L. Li, J.M. Hao, X.N. Li, C. Dong, and T.G. Nieh: *Acta Mater.*, 2018, vol. 147, pp. 213–25.
23. A. Munitz, S. Salhov, S. Hayun, and N. Frage: *J. Alloys Compd.*, 2016, vol. 683, pp. 221–30.
24. V. Shivam, J. Basu, V.K. Pandey, Y. Shadangi, and N.K. Mukhopadhyay: *Adv. Powder Technol.*, 2018, vol. 29 (9), pp. 2221–30, https://doi.org/10.1016/j.apt.2018.06.006.
25. C.M. Lin and H.L. Tsai: *Intermetallics*, 2011, vol. 19, pp. 288–94.
26. J. Hao, Y. Ma, Q. Wang, C. Zhang, C. Li, C. Dong, Q. Song, and P.K. Liaw: *J. Alloy Compd.*, 2019, vol. 780, pp. 408–21.
27. F. Meng, J. Qiu, and I. Baker: *Mater. Sci. Eng. A*, 2013, vol. 586, pp. 45–52.
28. J.Y. He, H. Wang, H.L. Huang, X.D. Xu, M.W. Chen, Y. Wu, X.J. Liu, T.G. Nieh, K. An, and Z.P. Lu: *Acta Mater.*, 2016, vol. 102, pp. 187–96.

29. H. Jain, Y. Shadangi, V. Shivam, D. Chakravarty, D. Mukhopadhya, N.K. Kumar, and V. Shivam: *J. Alloys Compd.*, 2020, vol. 834, p. 155013.
30. A.R. Miedema, P.F. de Châtel, and F.R. de Boer: *Phys. B*, 1980, vol. 100, pp. 1–28.
31. S. Guo and C.T. Liu: *Prog. Nat. Sci. Mater. Int.*, 2011, vol. 21, pp. 433–46.
32. M.J. Yao, K.G. Pradeep, C.C. Tasan, and D. Raabe: *Scr. Mater.*, 2014, vols. 72–73, pp. 5–8.
33. S. Ghosh, J. Basu, D. Ramachandran, E. Mohandas, and M. Vijayalakshmi: *Intermetallics*, 2012, vol. 23, pp. 148–57.
34. E.A. Marquis and D.N. Seidman: *Acta Mater.*, 2001, vol. 49, pp. 1909–19.
35. M.E. Thompson, C.S. Su, and P.W. Voorhees: *Acta Metall.*, 1994, vol. 42, pp. 2107–22.
36. B.. Murty: *High Entropy Alloy*, 2014.
37. J. Basu and S. Ranganathan: *Sadhana*, 2003, vol. 28, pp. 783–98.
38. J. Basu and S. Ranganathan: *Acta Mater.*, 2008, vol. 56, pp. 1899–1907.
39. J. Basu and S. Ranganathan: *Intermetallics*, 2009, vol. 17, pp. 128–35.
40. J. Basu and S. Ranganathan: *Intermetallics*, 2004, vol. 12, pp. 1045–50.
41. Y. Zhou, X. Jin, L. Zhang, X. Du, and B. Li: *Mater. Sci. Eng. A*, 2018, vol. 716, pp. 235–39.